Title

Osteosarcoma PDX-Derived Cell Line Models for Preclinical Drug Evaluation Demonstrate Metastasis Inhibition by Dinaciclib through a Genome-Targeted Approach

Journal

Clinical Cancer Research, 30(4)

ISSN

1078-0432

Authors

Schott, Courtney R
Koehne, Amanda L
Sayles, Leanne C
et al.

Publication Date

2024-02-16

DOI

10.1158/1078-0432.ccr-23-0873

Peer reviewed

Osteosarcoma PDX-Derived Cell Line Models for Preclinical Drug Evaluation Demonstrate Metastasis Inhibition by Dinaciclib through a Genome-Targeted Approach

Courtney R. Schott[1,2], Amanda L. Koehne[1], Leanne C. Sayles[1], Elizabeth P. Young[1], Cuyler Luck[1,3], Katherine Yu[1,3], Alex G. Lee[1], Marcus R. Breese[1], Stanley G. Leung[1], Hang Xu[4], Avanthi Tayi Shah[1], Heng-Yi Liu[1], Aviv Spillinger[1], Inge H. Behroozfard[1], Kieren D. Marini[1], Phuong T. Dinh[1], María V. Pons Ventura[1], Emma N. Vanderboon[2], Florette K. Hazard[5], Soo-Jin Cho[6], Raffi S. Avedian[7], David G. Mohler[7], Melissa Zimel[8], Rosanna Wustrack[8], Christina Curtis[4], Marina Sirota[1,3], and E. Alejandro Sweet-Cordero[1]

ABSTRACT

Purpose: Models to study metastatic disease in rare cancers are needed to advance preclinical therapeutics and to gain insight into disease biology. Osteosarcoma is a rare cancer with a complex genomic landscape in which outcomes for patients with metastatic disease are poor. As osteosarcoma genomes are highly heterogeneous, multiple models are needed to fully elucidate key aspects of disease biology and to recapitulate clinically relevant phenotypes.

Experimental Design: Matched patient samples, patient-derived xenografts (PDX), and PDX-derived cell lines were comprehensively evaluated using whole-genome sequencing and RNA sequencing. The *in vivo* metastatic phenotype of the PDX-derived cell lines was characterized in both an intravenous and an orthotopic murine model. As a proof-of-concept study, we tested the preclinical effectiveness of a cyclin-dependent kinase inhibitor on the growth of metastatic tumors in an orthotopic amputation model.

Results: PDXs and PDX-derived cell lines largely maintained the expression profiles of the patient from which they were derived despite the emergence of whole-genome duplication in a subset of cell lines. The cell lines were heterogeneous in their metastatic capacity, and heterogeneous tissue tropism was observed in both intravenous and orthotopic models. Single-agent dinaciclib was effective at dramatically reducing the metastatic burden.

Conclusions: The variation in metastasis predilection sites between osteosarcoma PDX-derived cell lines demonstrates their ability to recapitulate the spectrum of the disease observed in patients. We describe here a panel of new osteosarcoma PDX-derived cell lines that we believe will be of wide use to the osteosarcoma research community.

Introduction

Osteosarcoma is a rare malignant bone tumor most commonly diagnosed in children, adolescents, and young adults. The majority of patients have micrometastases at diagnosis, requiring the use of intensive adjuvant chemotherapy (1–3). Despite aggressive treatment, progression often presents as distant macrometastatic disease in the lungs or bone, and patients who develop metastases have a 5-year survival rate of 20% to 30% (3–7). Over the past several decades, there has been limited progress in identifying new therapies for patients with osteosarcoma and survival has not substantively improved, particularly for patients with metastatic disease (7–9). This lack of progress may be partly due to a paucity of models that accurately recapitulate osteosarcoma metastatic progression. Osteosarcoma genomes are characterized by multiple copy-number alterations, chromothripsis, and aneuploidy, resulting in significant heterogeneity in oncogenic drivers. Well-characterized models are crucial not only for elucidating mechanisms of metastasis but also for identification of new therapeutic strategies (10, 11).

While *in vitro* assays are often used to predict or inform on the metastatic capacity of neoplastic cells (e.g., invasion, migration, anoikis, etc.), *in vivo* modeling remains the gold standard to fully evaluate the metastatic cascade. Experimental metastasis models where cancer cells are disseminated after intravenous injection recapitulate the latter half of the metastatic cascade, including survival within the bloodstream, extravasation, tissue colonization, and tumor establishment. However, to model the full metastatic cascade, models that metastasize spontaneously from a relevant orthotopic site are required.

Only a limited number of established osteosarcoma cell lines have demonstrated the ability to consistently form metastases when injected

[1]Department of Pediatrics, University of California San Francisco, San Francisco, California. [2]Department of Pathobiology, Ontario Veterinary College, University of Guelph, Guelph, Ontario, Canada. [3]Bakar Computational Health Sciences Institute, University of California San Francisco, San Francisco, California. [4]Departments of Genetics and Medicine, Stanford University School of Medicine, Stanford University, Stanford, California. [5]Department of Pathology, Stanford University School of Medicine, Stanford University, Stanford, California. [6]Department of Pathology, University of California San Francisco, San Francisco, California. [7]Department of Orthopedic Surgery, Stanford University School of Medicine, Stanford University, Stanford, California. [8]Department of Orthopedic Surgery, University of California San Francisco, San Francisco, California.

Corresponding Author: E. Alejandro Sweet-Cordero, University of California San Francisco, 1550-4th Street, Rock Hall Rm 384D, San Francisco, CA 94143. E-mail: alejandro.sweet-cordero@ucsf.edu

Clin Cancer Res 2024;30:849–64

doi: 10.1158/1078-0432.CCR-23-0873

Translational Relevance

Metastasis continues to be the primary cause of death for patients with osteosarcoma. We expect that these patient-derived xenograft (PDX)-derived cell lines will be broadly useful to researchers investigating mechanisms of osteosarcoma metastasis as well as the preclinical development of therapies to treat metastatic disease. We sought to develop an orthotopic osteosarcoma model to fully evaluate the entire metastatic cascade as a clinically relevant model for preclinical testing. The two most aggressive cell lines described form invasive orthotopic xenografts that reach the amputation endpoint in < 6 weeks and metastasize to lung, liver, bone, and other sites less than 1 month postamputation; these latency characteristics make this an appealing model for mechanistic studies and preclinical therapeutic development. The variation in metastasis predilection sites between osteosarcoma PDX-derived cell lines illustrates the ability of these models to recapitulate the spectrum of the human disease.

intravenously (refs. 12–20; Supplementary Table S1). To develop additional models, prior work has sought to increase metastatic capacity by exposure to carcinogens, introduction of oncogenes, or serial passaging of established osteosarcoma cell lines through mice (14, 15, 21–27). These strategies have successfully enhanced the metastatic capacity of several osteosarcoma cell lines in both intravenous and orthotopic models (12, 14). However, these approaches may introduce alterations that are not reflected in endogenous human metastasis. Furthermore, murine orthotopic osteosarcoma models are most commonly generated by implanting tumor cells/tissue into the epiphyseal bone or onto the periosteal surface of the tibia (12, 16, 33–41, 19, 20, 27–32). However, injecting tumor cells/tissue directly into the bone can lead to immediate exit through the vasculature, essentially skipping the initial stages of the metastatic cascade and seeding the lungs directly (42–45). The periosteal implantation strategy to model spontaneous metastasis requires tumor cells to invade through the cortex without risk of inadvertently introducing cells into the vasculature at implantation. Models incorporating amputation of the affected limb, provide additional time for the development of metastases in the lungs or other organs (12, 16, 29, 32, 41). Because surgical removal of the primary tumor is a component of the standard of care for patients with osteosarcoma, inclusion of primary tumor removal in a mouse model more closely recapitulates management of the human disease.

The use of patient-derived xenografts (PDX) to model cancer enhances the probability of retaining key features of the human disease (11, 42, 46–49). However, only a limited number of osteosarcoma PDXs have been evaluated for metastatic potential *in vivo* (31, 41, 42, 50, 51). Cell lines generated from PDXs may also be useful to establish more consistent and more tractable models for the exploration of molecular pathogenesis and for testing novel therapeutic drugs for pediatric osteosarcoma compared with established commercially available cell lines, many of which have been in culture for decades (52).

To enable the development of new models to study osteosarcoma metastasis, we generated PDXs from clinically annotated patient tumors. Cell lines were then generated from the PDXs and rigorously characterized *in vivo* using both an intravenous and an orthotopic model (**Fig. 1**). Whole-genome sequencing (WGS) and RNA sequencing (RNA-seq) were used to evaluate consistency between the PDXs and the patient tumor from which they were derived. Here, we describe the *in vivo* features of these novel PDX-derived cell lines including tumorigenicity and metastatic capacity in both tail vein intravenous and paratibial orthotopic amputation models. Bioluminescence imaging (BLI) was used to quantify whole body metastatic burden, while IHC was used to aid quantification of metastatic tumor burden in the lung and liver. To demonstrate the utility of PDX-derived cell lines for preclinical testing, we performed a proof-of-concept study which showed that a cyclin-dependent kinase (CDK) inhibitor decreased metastatic tumor growth of a *MYC*-amplified cell line after

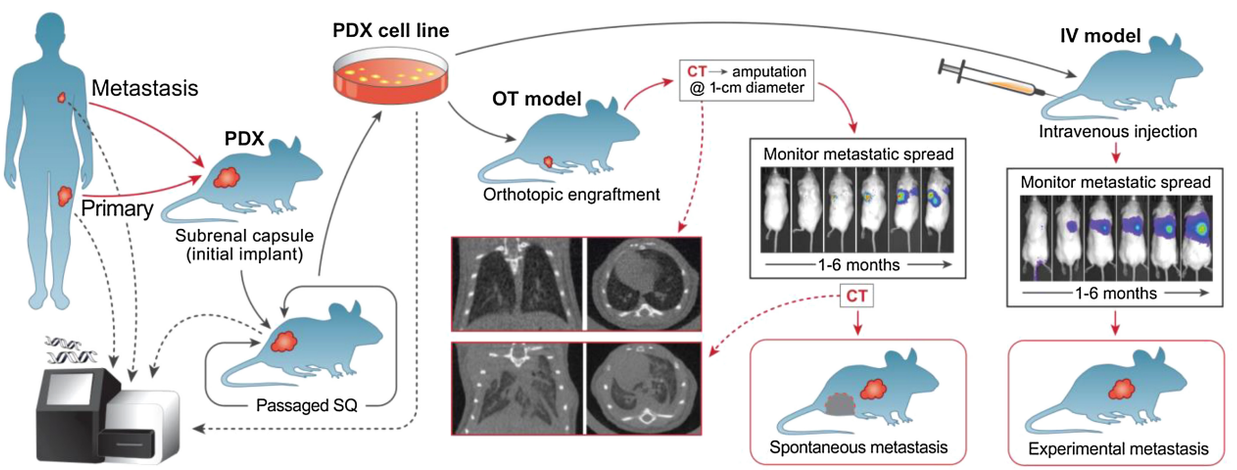

Figure 1.
Modeling pediatric osteosarcoma metastasis *in vivo* using well-characterized PDX-derived cell lines. Schematic diagram outlining the generation of PDXs from primary and secondary pediatric osteosarcoma. PDX-derived cell lines are generated from PDXs, then both WGS and RNA-seq are performed on matched patient, PDX, and PDX-derived cell line samples. These cell lines are characterized for their metastatic capacity and tissue trophism *in vivo* using intravenous and orthotopic amputation murine models with dynamic monitoring of metastatic burden using BLI.

amputation of an orthotopic xenograft. We expect that these PDX-derived cell lines will be broadly useful to researchers investigating mechanisms of osteosarcoma metastasis as well as the preclinical development of therapies to treat metastatic disease.

Materials and Methods

Patient sample procurement

All samples were reviewed by a pathologist (F.K. Hazard or S.J. Cho) and the diagnosis was confirmed as osteosarcoma. Samples were received fresh and were grossly evaluated by a pathologist (F.K. Hazard or S.J. Cho) for viable tumor tissue. A representative sample was reserved for PDX implantation and the remainder of the sample was flash-frozen for DNA/RNA extraction.

PDX and cell line generation

For PDX generation, 1 mm^3 fragments of fresh or frozen-thawed patient tumor were dipped in Matrigel (Corning) and implanted under the renal capsule of NSG mice. Mice were monitored for tumor growth by abdominal palpation for up to 1 year postimplantation. Successfully engrafted tumors were allowed to reach 1 to 2 cm^3 before the mouse was euthanized and tumor harvested. Tumors were digested in a collagenase buffer and filtered through a 70-μm filter. For PDX passaging, cells were implanted subcutaneously in the flank of NSG mice (5×10^5 cells) in 30 μL of MEM alpha and 20 μL Matrigel. PDX-derived cell lines were generated as described previously (11).

Sequencing

Flash-frozen patient tumors, PDXs, and PDX-derived cell lines were placed into 1.5-mL tubes on ice and disrupted with a plastic tissue homogenizer. Demineralization was not required. Tumors were digested to a single cell suspension in collagenase digest buffer and sorted for human cells using anti-human HLA-ABC (BioLegend, 555555). DNA and RNA were extracted using an AllPrep Kit (Qiagen, 80204) with QIAshredder (Qiagen, 79654). RNA was quantified with a Nanodrop 2000c (Thermo Fisher) and RNA integrity was analyzed on an Agilent 5200 Fragment Analyzer. RNA-seq was performed as described previously (11).

RNA-seq

Hierarchical clustering

Fastq files and counts were derived using STAR (2.5.3a; RRID: SCR_004463) with the hg38 index (53). Normalized values were calculated using the edgeR package (RRID:SCR_012802) as log CPM with prior count set to 2 (54). ComBat (RRID:SCR_010974) was then used as a batch correction for the sample source (patient, PDX, or cell line; ref. 55). The top 80th percentile most variant genes (based on coefficient of variance) were used for hierarchical clustering using the Manhattan method for distance followed by the Ward.D2 agglomeration method.

MYC-amplified sample analysis

Log_2 [transcript per million (TPM) + 1] values were derived from hg38 human index using the UCSC Toil RNA-seq workflow (56) and copy-number assignments (described under *Whole-genome sequencing and allele-specific copy-number analysis*). Groups were classified as High *MYC* and Low *MYC* based on their *MYC* expression: values exceeding 50 percentile were designated as High *MYC*, while those below 50 percentile were considered Low *MYC*. Differentially expressed genes were identified utilizing the limma-voom linear model, incorporating empirical Bayes moderation (57). Genes meeting the criteria of a P value < 0.05, abs [log fold change (FC)] > 1, and a FDR < 0.05 were considered as significantly expressed.

Gene set enrichment analyses were performed using the fgsea R package (58), based on pathways downloaded from MSigDB (RRID: SCR_016863). Genes were ranked according to their logFC between High *MYC* and Low *MYC*, and a running-sum statistic was used to calculate enrichment scores for each gene set/pathway. These scores were then normalized to account for the size of each set, resulting in normalized enrichment scores (NES). P values and FDR were derived from a permutation test to assess the statistical significance of the NES.

Data acquisition

TARGET (from Genomic Data Commons Data Portal RRID: SCR_014514) and Cancer Cell Line Encyclopedia (CCLE; RRID: SCR_013836) TPM data were downloaded from the UCSC Treehouse Public Data repository (https://treehousegenomics.soe.ucsc.edu/public-data/). For the TARGET dataset, Tumor Compendium v10 Public PolyA TPM expression and clinical datasets released in July 2019 were used and were filtered for osteosarcoma TARGET samples. For CCLE, the Cell Line Compendium v2 TPM expression and clinical datasets released in December 2019 were downloaded and filtered for osteosarcoma cell lines. Patient tumor samples from which cell lines were also derived were excluded from the analysis.

The samples from TARGET, CCLE, and our dataset were processed using the UCSC Toil RNA-seq pipeline (https://github.com/BD2KGenomics/toil-rnaseq) and the RSEM TPM values were used in the correlation analysis. For CCLE and our cell line data, the Toil pipeline was used in-house to generate RSEM gene-level Hugo counts for differential gene expression analysis (56).

Correlation analysis

The correlation analysis was performed as described by Yu and colleagues (59). Briefly, the 5,000 most variable protein-coding genes by interquartile range (IQR) were selected across the osteosarcoma patient samples. These genes were used to calculate the Spearman's correlation coefficient for each patient sample (TARGET and Sweet-Cordero lab) compared with each cell line (CCLE and PDX-derived cell lines). Patient-to-cell line correlations for CCLE cell lines versus PDX-derived cell lines were compared using the Wilcoxon rank-sum test.

WGS and allele-specific copy-number analysis

A list of clinically actionable genes was generated by combining the gene lists from several cancer-related gene panels: FoundationOne and FoundationOne Heme (combined, Foundation Medicine, list accessed May 31, 2017), MSK-IMPACT (60), Mi-oncoseq (61), and UCSF 500 cancer gene panel (http://cancer.ucsf.edu/research/molecular-oncology/ucsf500). Genes present in more than one panel were included in an "actionable" gene list. Actionable genes that also had a drug interaction listed in the Drug Gene Interaction Database (DGIdb; accessed June 13, 2018; RRID:SCR_006608; ref. 62) were included in the actionable/druggable gene list, and this gene list was used to identify recurrent somatic copy number. Alignment of FASTQ files, somatic variant calling, and structural variant calling was performed as previously described (11). Copy-number analysis and purity correction was also performed as previously described (11), with the difference of allele-specific copy number being calculated using the B-allele frequency (BAF) based upon germline variant allele frequency (VAF). For samples without germline data available, population-level common SNPs were obtained from dbSNP and used as an alternative to patient-specific germline variants. Concordance of copy number across the

genome was calculated by tallying the fraction of the genome with the same integer copy-number value between related samples. Concordance was calculated separately for major and minor alleles. Major copy-number gain is defined as >8 copies and minor is defined as 4 to 8 copies. For copy-number losses, <1.2 copies defines minor and <0.8 copies defines major.

Somatic variant calling and circos plot generation

Single-nucleotide variants and small-scale insertions/deletions were called using Mutect2 (GATK v3.8; RRID:SCR_001876; refs. 63, 64) and Strelka (v2.9.10; RRID:SCR_005109; ref. 65). To filter out low-confidence calls, only the variants having at least four supporting reads and called by both Mutect2 and Strelka were retained. In addition, a variant was considered a true positive when the VAF was greater than 5%, the sequencing depth was ≥20, and there were ≥3 sequence reads supporting the variant call. Somatic structural variants were called from WGS data by combining the output of Manta (v1.6.0; RRID:SCR_022997; ref. 66), DELLY (v0.8.1; RRID:SCR_004603; ref. 67), GRIDSS (v2.9.4; ref. 68), and SvABA (v.1.1.3; RRID:SCR_022998; ref. 69). Consensus calls were made by comparing the output of GRIDSS and the other three tools, with a maximum allowed distance of 100 bp as measured pairwise between breakpoints. Two approaches were used to estimate the copy-number profile, ploidy, and purity of a tumor sample from matched normal and tumor WGS data. Approach one implements PURPLE (v3.0; RRID:SCR_022999) which combines BAF from AMBER (v3.3; RRID:SCR_016151), read depth ratios from COBALT (v1.8; RRID:SCR_004152), somatic variant and structural variant calls. Approach two implements alleleCount (v4.2.1) (https://github.com/cancerit/alleleCount) for allele counting and ascatNgs (70, 71) for estimating tumor purity, ploidy, and copy-number profile. Manual inspections were taken when there was a discrepancy between the two approaches. Circos plots were generated using PURPLE (v3.0) to plot final somatic copy-number calls, point mutation calls, and structural variation calls.

Cell culture

Mycoplasma testing and STR analysis (Supplementary Table S2) were performed on cell lines prior to *in vitro* and *in vivo* use. Eight PDX-derived cell lines (**Table 1**) and three established commercially available cell lines were used for the *in vivo* studies. SJSA (RRID:CVCL_1697) and MG63 (RRID:CVCL_0426) were obtained from the American Type Culture Collection. MG63.3 (RRID:CVCL_WL01) was a gift from Dr. Robbie Majzner (Stanford University). All cells were maintained in a 37°C 5% CO_2 humidified incubator and cultured in standard DMEM media (Corning) supplemented with 10% bovine growth serum (Hyclone SH30541.03) and 1% penicillin–streptomycin–glutamine. Stable luciferase-expressing cell lines were generated using lentiviral transduction (RRID:Addgene_39196) followed by sorting for GFP using a Sony Biotechnology SH800S Cell Sorter (RRID:SCR_018066).

For the cell proliferation assay, cells were seeded in a 96-well plate and allowed to attach overnight. Plates were transferred into an Incucyte S3 Live-Cell Analysis System (Sartorius, RRID:SCR_023147), and whole-well images were collected every 8 hours until wells reached 100% confluence. Incucyte software (Incucyte S3 2019A) was used to create confluence masks for each cell line. Confluence over time was used to identify a period of exponential cell growth and the linear portion of the curve was used to calculate doubling time in R statistical analysis software (72).

In vivo studies

For each cell line, a minimum of 4 mice were used for establishment of model endpoint timing. Luciferase-expressing cell lines were used for all PDX-derived cell lines and SJSA. Both parental and luciferase-expressing cell lines were used for a subset of cell lines (OS052, OS152, OS186, and OS526). Only the parental version was used for MG63 and MG63.3. For experimental metastasis studies, 1×10^6 cells were injected via the lateral tail vein in 100 μL of phosphate buffered saline (PBS); 1×10^5 cells were used for SJSA. For luciferase-expressing cell lines, BLI was performed every 28 days to monitor metastatic progression using a Perkin Elmer IVIS Spectrum In-Vivo Imaging System (RRID:SCR_020397). On the basis of worsening clinical signs associated with metastases and/or BLI signal intensity, an endpoint for each cell line model was determined.

To model spontaneous metastasis, paratibial orthotopic implantation followed by limb amputation was employed. At implantation, the periosteum of the medial aspect of the mid-tibia was gently scored with a 30-gauge needle prior to injecting 1×10^6 cells, 1×10^5 for SJSA, in 10 μL of Matrigel. After initial xenograft detection, tumor growth was monitored with twice-weekly measurements until the limb diameter reached 1 cm, when the affected limb was amputated by coxofemoral disarticulation. Prior to amputation, limb and lung microCTs were performed using the Perkin Elmer Quantum GX2 microCT Imaging System; a pulmonary microCT was also performed prior to euthanasia. If no xenograft could be identified within 6 months of implantation,

Table 1. Osteosarcoma PDX-derived cell line patient origin details, genomic features, and *in vivo* characteristics.

	Patient				Cell Line				Met *in vivo*		Xenograft	
ID	Age (yr)	Sex	Met @ Dx	Met Development	Origin	Tx Status	Site Origin	Genomic Feature	IV	OT	Take	Days to Amp
OS052	17	F	Yes - lung	N/A	primary	treated	fibula	*PTEN* loss	100%	22%	100%	35
OS152	11	F	No	Yes - lung & bone	metastatic	treated	scapula	*MYC* amplification	100%	100%	100%	39
OS186	13	M	Suspected	Yes - lung & bone	metastatic	treated	mandible	*MYC* & *CCNE1* amplification	0%	0%	100%	83
OS384	12	F	No	No @ 71 months	primary	treated	tibia	*VEGFA* amplification	100%	88%	100%	119
OS457	17	M	Yes - lung	N/A	primary	naïve	humerus	*CCNE1* amplification	0%	N/A	0%	N/A (>168)
OS525	20	F	Yes - lung	N/A	metastatic	treated	lung	*AKT1* amplification	100%	100%	100%	53
OS526	13	M	Yes - lung	N/A	primary	naïve	tibia	*CCNE1* amplification	100%	0%	100%	144
OS742	8	F	No	Yes - bone	primary	naïve	tibia	*MYC* & *CDK4* amplification	100%	100%	100%	30
OS766	30	F	Suspected	Yes - lung & bone	metastatic	treated	femur	*CDK4* amplification	TBD	TBD	TBD	TBD
OS833	14	M	No	Yes - lung	primary	treated	fibula	*MYC* amplification	TBD	TBD	TBD	TBD

Abbreviations: Amp, amputation; Dx, diagnosis; IV, intravenous; Met, metastasis; N/A, not applicable; OT, orthotopic; TBD, to be determined; Tx, treatment.

the cell line was deemed non-tumorigenic. Amputated limbs were demineralized in Immunocal (StatLab) for 24 hours prior to longitudinal bisection for histologic processing. An endpoint for each cell line was determined as it was for the intravenous model. Mice were euthanized 1 to 6 months, cell line dependent, post-injection for the intravenous model or postamputation for the orthotopic model.

For the dinaciclib study, luciferase-expressing OS152 cells were implanted orthotopically, as described above. BLI was performed initially 3 days postamputation and dinaciclib treatment commenced the following day. All mice received treatment for 3 weeks at 20 mg/kg 5 times/week intraperitoneally, and BLI was performed every 7 days. Dinaciclib powder (MedChemExpress) was dissolved in DMSO to 50 mg/mL for stock solution. For working solution, the stock was diluted to 2.5 mg/mL with 20% beta cyclodextrin in PBS immediately before injection. Mice were weighed weekly. BLI signal was tracked over time using Living Image software (Perkin Elmer; RRID: SCR_014247). BLI signal at endpoint was log-transformed and means were compared between the vehicle and control groups with a two-tailed *t* test, after testing for normality. Differences were considered significant when $P < 0.05$.

For all *in vivo* studies, lungs, liver, and tissue from additional metastatic sites were harvested for histologic evaluation and metastatic burden analysis. Prior to collection, 5 mL of PBS was injected into the right ventricle of the heart and the lungs were inflated with 1 mL of formalin via the trachea. Tissues were fixed for 24 to 48 hours in formalin and then transferred to 70% ethanol prior to histologic processing.

IHC

IHC was performed on formalin-fixed, paraffin-embedded tissue mounted on glass slides. Standard heat-induced epitope retrieval using sodium citrate buffer (pH 6.0) was performed prior to H_2O_2 quenching of endogenous peroxidase activity. Blocking and antibody dilutions were made in 5% normal horse serum (Vector Labs), and slides were incubated overnight at 4°C in a humidified chamber with anti-human mitochondria antibody (1:1000; Abcam, catalog no. ab92824, RRID:AB_10562769). Slides were incubated in secondary horse anti-mouse antibody (Vector Labs) and avidin-biotin (Vectastain Elite ABC kit) for 30 minutes each at room temperature. Signal was developed with a DAB substrate kit (Abcam, catalog no. ab64238).

Slide scanning and image analysis

Histology slides were scanned by the UCSF Histology & Biomarker Core at 10x using the Zeiss Axio Scan.Z1 Digital Slide Scanner (RRID: SCR_020927). Scanned slides were imported into QuPath Quantitative Pathology & Bioimage Analysis software (RRID:SCR_018257). Tissue was outlined using simple tissue detection prior to manual correction to exclude shadows, debris, and other tissue regions not meant for analysis. Training images were created from multiple regions across a selection of slides and were used to train the pixel classifier to identify DAB positive tissue. The pixel classifier was used to create tumor annotations across all slides with a minimum object size of 250 μm^2. All annotations were checked manually for accuracy prior to quantification of tumor burden.

Statistics

Metastatic burden was compared between the treatment and control groups with a two-tailed *t* test for normally distributed data and the Mann–Whitney test for non-normally distributed data. Differences were considered significant when $P < 0.05$.

Study approval

Written informed consent was collected from all patients or parents in the case of patients less than 18 years old. Using established guidelines (Belmont Report), institutional review board approval was granted from each participating institution (73). All procedures involving mice were conducted in accordance with protocols approved by the UCSF Institutional Animal Care and Use Committee.

Data availability

The sequence data generated by the authors and analyzed in this study are publicly available in database of Genotypes and Phenotypes (dbGAP) at phs002430. Other sequence data analyzed in this study were obtained from TARGET and CCLE at https://treehousegenomics.soe.ucsc.edu/public-data/#tumor_v10_polyA and https://treehousegenomics.soe.ucsc.edu/public-data/previous-compendia.html#cell_line_v2.

Results

Osteosarcoma PDXs are highly similar to their patient of origin

Tumor samples obtained from diagnostic biopsies, post-chemotherapy primary resections, or metastases, were collected directly from patients at the time of surgery with institutional review board approval and appropriate consent. Tumor fragments were implanted into the subrenal capsule of NSG mice to generate PDXs. PDXs retain the morphological features of their respective patient tumor based on histology (11), even over multiple passages (Supplementary Fig. S1). From these PDXs, we generated eleven PDX-derived cell lines. Of these cell lines, three were obtained from pretreatment biopsies, three from posttreatment resections, and four from distant metastasis (**Table 1**).

Where feasible, fresh-frozen tumor samples were analyzed by WGS and RNA-seq. WGS and RNA-seq was also performed for all PDXs and PDX-derived cell lines (**Figs. 2** and **3**; Supplementary Table S3). Unsupervised hierarchical clustering of RNA-seq data demonstrated remarkable similarity of the patient tumor to the corresponding PDX and PDX-derived cell line (**Fig. 3A**). In contrast, most established commercially available osteosarcoma cell lines (HOS, 143B, SJSA, U2OS, MG63, and MG63.3) clustered separately from our cohort of patient samples, PDXs, and PDX-derived cell lines (**Fig. 3A**). Thus, over decades of *in vitro* passaging, these established commercially available cell lines may have drifted away from patient samples, providing support for the hypothesis that newly derived PDX-derived cell lines retain key features of the gene expression programs of primary tumors. Next, we compared the gene expression profiles of PDX-derived cell lines and established commercially available cell lines to patient primary tumor samples from publicly available data (**Fig. 3B** and **C**). Overall, the PDX-derived cell lines had a higher correlation to human osteosarcoma patient samples that was statistically significant (Supplementary Fig. S2A). Across all cell lines tested, the three with the highest mean correlation to human osteosarcoma patient samples were PDX-derived cell lines (**Fig. 3B**).

Osteosarcoma is genomically complex, with widespread aneuploidy and structural rearrangements (7, 74). We previously described comparison of a limited panel of osteosarcoma PDXs to their corresponding tumor of origin (11). Here we sought to characterize the changes that occurred at the genomic level when comparing this new collection of PDX-derived cell lines to their matched patient and PDX samples. We compared the copy-number profile of patient tumors and their corresponding PDXs and PDX-derived cell lines. Overall, we found a

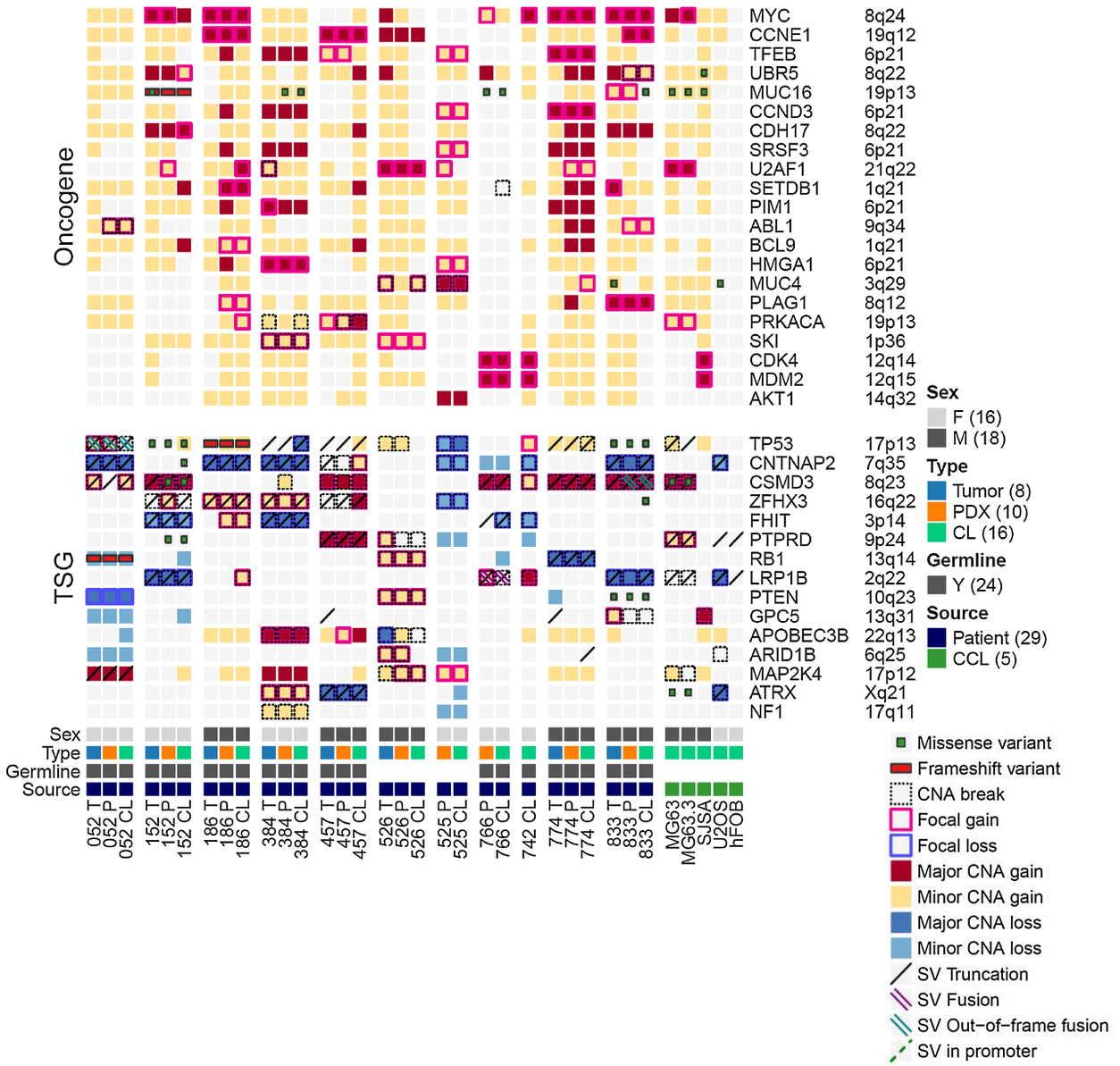

Figure 2.

WGS of patients, PDXs, and PDX-derived cell lines. Oncoprint showing the genomic alterations in oncogenes and tumor suppressor genes (TSG) across primary tumors (T), PDXs (P), PDX-derived cell lines (CL), and commercially available cell lines. Alterations in top recurrently altered and certain selected oncogenes and tumor suppressors are shown. Focal copy-number alterations are defined as contiguous segments of similar copy-number change less than 1 Mb in length. Structural variant (SV) fusion calling and frameness determined using WGS only without RNA-seq confirmation.

high degree of concordance of copy-number profiles as identified by WGS (Supplementary Fig. S2B and S2C). In two of the cell lines tested *in vivo* (OS457 and OS186), whole-genome duplication (WGD) led to a wider degree of difference compared with the tumor of origin as quantified by the percentage of genome segments overlapping with regards to copy number (Supplementary Fig. S2B). In one case (OS457), the WGD appears to have occurred in the establishment of the PDX (Supplementary Fig. S2B). In the second case (OS186), the WGD occurred sometime after the establishment of the PDX-derived cell line (Supplementary Fig. S2B). Similarly, Circos plots demonstrated high similarity in the structural rearrangements between patient, PDX, and PDX-derived cell line (Supplementary Fig. S3).

Metastatic capacity of osteosarcoma PDXs is highly variable

Next, we evaluated the metastatic capacity of the PDXs *in vivo*. Differences in metastatic potential was assessed using several different methods. Lungs from a subset of mice harboring subcutaneous xenografts, during PDX generation and passaging, were evaluated for the presence of spontaneous metastasis. We also characterized the ability of a subset of these PDXs to form metastases after intravenous

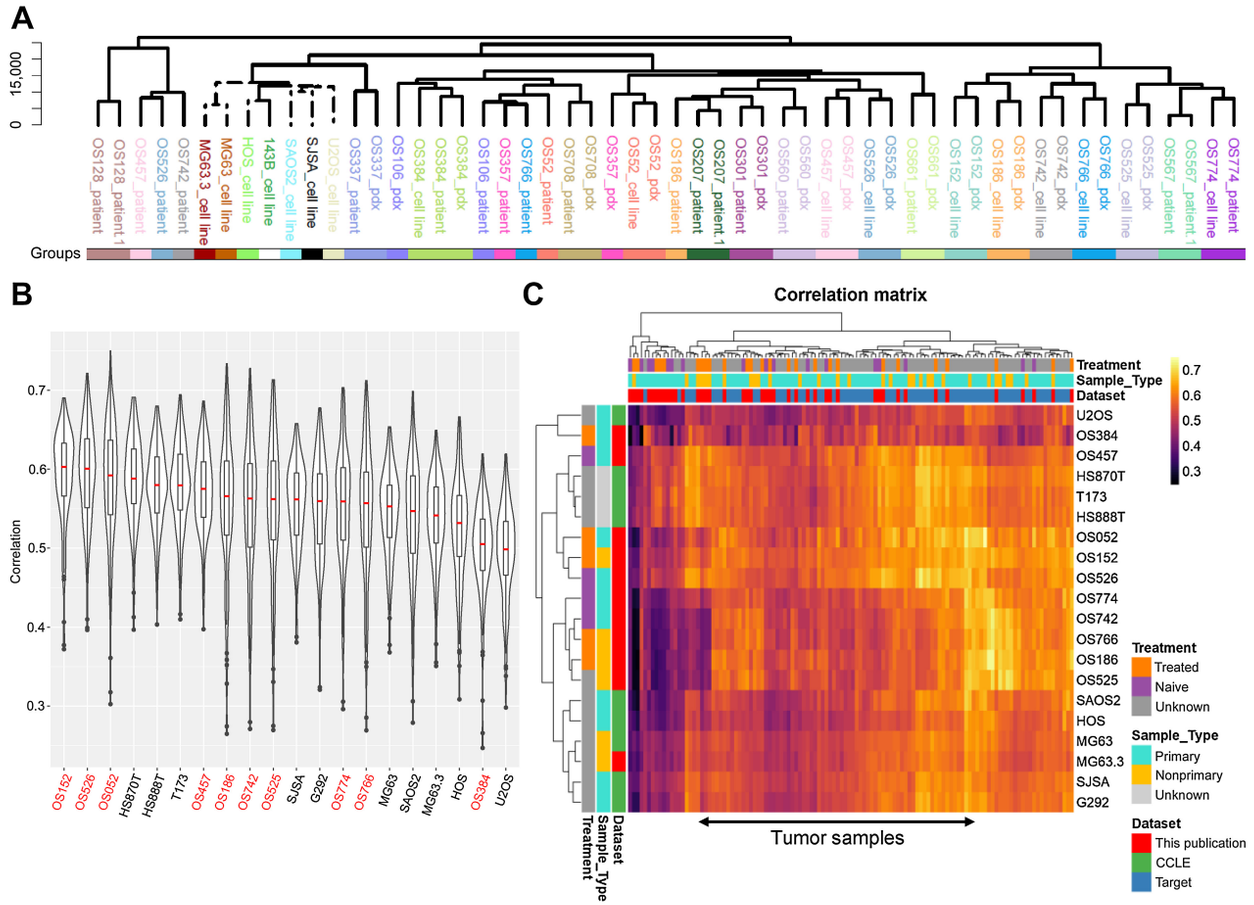

Figure 3.

Sequencing of patients with osteosarcoma, PDXs, and PDX-derived cell lines. **A,** Hierarchical clustering of RNA-seq data from osteosarcoma patient tumors, PDXs, PDX-derived cell lines, and established commercially available cell lines. Patient tumors and their corresponding PDX and PDX-derived cell line exhibit remarkable similarity and cluster separately to established commercially available cell lines. **B,** Gene expression of osteosarcoma PDX-derived cell lines correlates with osteosarcoma patient tumors. Violin plot of Spearman's correlations between all possible pairs of primary patient tumor samples (CCLE and Sweet-Cordero lab) and either established commercially available osteosarcoma cell lines (CCLE and Sweet-Cordero lab) or PDX-derived cell lines using the 5,000 most variable genes, separated by individual cell lines (*x*-axis). Names of the PDX-derived cell lines are in red and names of cell lines from the CCLE are in black. The median correlation coefficients are depicted by the red center line and the overlaid boxplots depict the upper and lower quartiles, with the whiskers depicting 1.5 times the IQR. **C,** Heatmap showing the Spearman's correlations between osteosarcoma cell lines (rows) and primary tumor samples (columns). The color annotation bars on the x- and y-axis indicate the treatment status, tumor type (e.g., primary, nonprimary, unknown), and dataset of each sample.

injection. Lungs were collected at the time of PDX passaging for mice with subcutaneous PDX implants and 28 days post-injection for mice injected with PDX cells intravenously. Evidence of metastasis was evaluated histologically revealing the presence of both micro- and macro-metastases (Supplementary Fig. S4A–S4C). Of the PDXs evaluated for spontaneous metastasis from subcutaneous tumors, eight of eleven demonstrated the ability to form lung metastasis (Supplementary Fig. S4B). When injected intravenously, three of five PDXs induced lung metastasis (Supplementary Fig. S4C). We observed some discordance in the ability of certain PDXs to form metastasis during subcutaneous passaging versus in the intravenous model. For example, OS128 induced metastasis in the intravenous model but not during subcutaneous passaging, while OS152 and OS186 metastasized during subcutaneous passaging but not after intravenous administration (Supplementary Fig. S4B and S4C).

Osteosarcoma PDX-derived cell lines form metastases when injected intravenously

As we noted a high degree of correlation at the level of transcription between the PDX and the PDX-derived cell lines (**Fig. 3A**), we reasoned that the latter would be a more tractable model system for metastatic studies. To assess the metastatic capacity of osteosarcoma PDX-derived cell lines *in vivo*, PDX-derived cell lines were transduced with a lentiviral vector expressing luciferase to facilitate dynamic monitoring of metastatic burden in NSG mice. We first determined that proliferation rates between luciferase-expressing PDX-derived cell lines and the parental version were similar (Supplementary Fig. S5A). Next, cells were introduced via the lateral tail vein and mice were monitored with BLI to estimate whole body metastatic burden (**Fig. 4A**). Most (6/8) osteosarcoma PDX-derived cell lines tested generated metastases with increasing BLI signal over time (**Fig. 4B** and **C**; Supplementary Fig. S6A–S6H). Study duration for

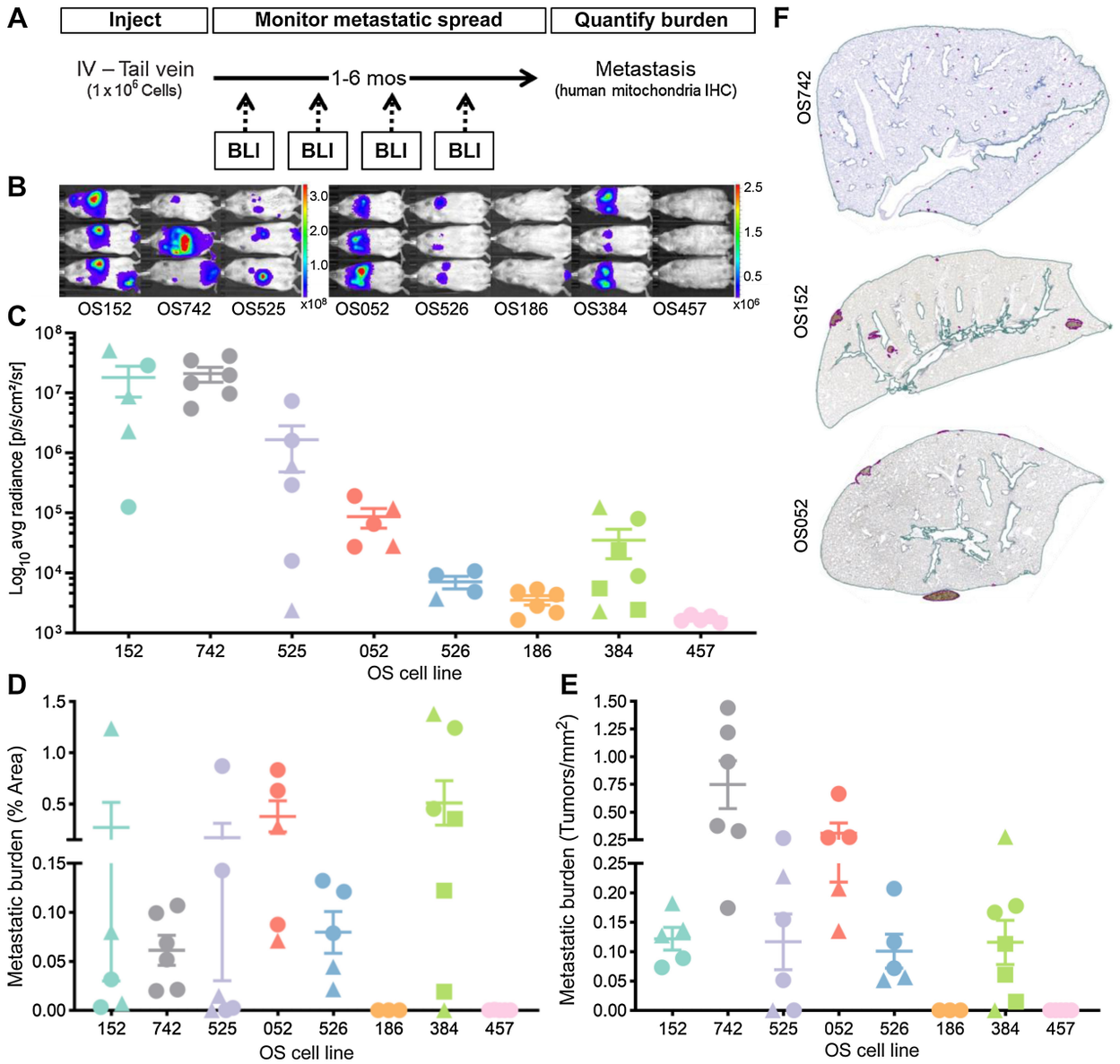

Figure 4.

Osteosarcoma PDX-derived cell lines metastasize after intravenous injection. Intravenous metastatic capacity was determined by injecting 1×10^6 cells into the lateral tail vein of 2- to 5-month-old NSG mice. For all graphs, within each cell line, mice implanted at the same time are represented by the same symbol. **A,** Intravenous model schematic: after intravenous injection, mouse health was monitored for clinical signs associated with metastasis and BLI was performed monthly to estimate burden to determine study endpoint for each cell line. At endpoint, tissues were harvested for quantitative burden analysis using human mitochondria IHC. **B,** Metastatic burden varied between cell lines. Representative images from 3 mice per cell line of the BLI signal at endpoint representing total tumor burden from all sites. BLI color scale is in radiance (photons/sec/cm^2/sr); left scale: Min = 3.12×10^6 and Max = 3.31×10^8 and right scale: Min = 2.94×10^4 and Max = 2.58×10^6. **C,** Total BLI signal at endpoint, ordered from fastest to slowest time to endpoint, for all mice for each PDX-derived cell line. **D** and **E,** Cell lines most frequently metastasized to lung. Metastatic burden quantification of lung tissue immunolabeled with human mitochondria antibody for overall tumor area (**D**) and number of tumors per mm^2 (**E**) for individual mice. **F,** Tumor size and distribution in the lung parenchyma varied between cell lines. Microscopic images of lung lobes immunolabeled with human mitochondria antibody demonstrating metastatic burden for three PDX-derived cell lines. Tissue outlined in teal and tumors outlined in purple.

each cell line ranged from one to a maximum of 6 months and exhibited a trend of being inversely correlated with BLI signal at endpoint (**Table 2** and **Fig. 4B** and **C**). A subset of the parental (non–luciferase-expressing) PDX-derived cell lines were also evaluated using the intravenous model (Supplementary Fig. S5B–S5E and Supplementary Table S4).

A wide range of tropism with regards to metastatic sites was observed (**Table 2**). All six metastatic PDX-derived cell lines induced

Table 2. Osteosarcoma PDX-derived cell line *in vivo* intravenous study summary table.

		OS152	OS742	OS525	OS052	OS526	OS186	OS384	OS457
# Mice Total [# Studies]		5 [2]	6 [1]	6 [2]	5 [2]	5 [2]	6 [2]	6 [3]	5 [1]
Endpoint (avg days)		53	55	80	85	140	160	168	168
Endpoint Decision with CS, if Applicable		BLI, CS abd mass	BLI, CS low BCS, gait	CS paralysis	BLI N/A	BLI N/A	max N/A	max N/A	max N/A
Metastatic Sites (%)	Lung	100	100	67	100	100	N/A	100	N/A
	Bone	20	33	100	20	0	—	0	—
	Liver	60	100	67	0	0	—	0	—
	Other	20	33	33	20	0	—	0	—

Abbreviations: abd, abdominal; avg, average; BCS, body condition score; CS, clinical signs.

pulmonary metastases: 5/6 metastasized consistently to lung in every mouse and 1/6 did so frequently (67%; **Table 2** and **Fig. 4D–F**). Lung metastases tended to be more frequent and larger in size toward the pleural surface (**Fig. 4F**). Four cell lines metastasized to bone (spine, sternum, rib, skull, and long bone) in 20% to 100% of mice per PDX-derived cell line. Lung and bone are the two most common sites of metastasis in patients with osteosarcoma. Liver metastasis (which is uncommon in patients) was also observed for three PDX-derived cell lines in the intravenous model (Supplementary Fig. S7A–S7C), although never in isolation. The non-luciferase versions that were tested metastasized to the same sites as BLI enabled lines with minor differences in location and burden (Supplementary Fig. S5B–S5E and Supplementary Table S4). The three most aggressively metastatic cell lines (OS152, OS742, and OS525) formed metastases in all mice tested, resulting in the highest overall burden, greatest number of sites, and shortest latency compared with the remaining PDX-derived cell lines (**Table 2**; **Fig. 4**; Supplementary Figs. S6–S7). With most PDX-derived cell lines demonstrating the ability to metastasize in an intravenous model with high incidence but low burden, we next tested their capacity to spontaneously metastasize in an orthotopic amputation model.

Osteosarcoma PDX-derived cell lines are tumorigenic in an orthotopic model

We sought to develop an orthotopic osteosarcoma model to fully evaluate the entire metastatic cascade as a clinically relevant model for preclinical testing. Paratibial implantation of luciferase-expressing PDX-derived cells into NSG mice was performed to assess tumorigenicity and capacity for spontaneous metastasis (**Fig. 5A**). All but one PDX-derived cell line (OS457) formed xenografts within 6 months of implantation (**Fig. 5B**; Supplementary Fig. S8A–S8H). This cell line was the most divergent from both the patient tumor and PDX from which it was derived, likely due to a WGD event that occurred while the cell line was established from the PDX (Supplementary Fig. S2B). Time to amputation (when the xenograft reached 1 cm in diameter), ranged from less than 1 month to 8 months for individual mice whereas average time to amputation for each cell line ranged from 1 to 5 months (**Table 3**; **Fig. 5B**; Supplementary Fig. S8A–S8G). Each tumorigenic PDX-derived cell line demonstrated a consistent growth rate for orthotopic xenografts except OS384 which varied widely (**Fig. 5B**; Supplementary Fig. S8G). For another PDX-derived cell line (OS457), BLI signal was detected after 6 months at the orthotopic implant site for all mice (Supplementary Fig. S8I), but no xenografts could be palpated nor were they captured histologically. PDX-derived cell line xenografts exhibited heterogeneous histologic phenotypes (Supplementary Fig. S8J), similar to what is seen in human patients. Most PDX-derived cell line xenografts exhibited regions with similar histologic phenotypes to the patient tumors from which they were derived (Supplementary Fig. S8J).

Cell line xenograft growth was similar regardless of the presence of luciferase, with a tendency for the luciferase-expressing version to reach amputation more slowly after implantation (Supplementary Fig. S9A–S9D). microCT prior to amputation detected tibial osteolysis and medullary cavity or trabecular bone invasion for all tumorigenic PDX-derived cell line xenografts in the orthotopic model, which was confirmed histologically (**Fig. 5C**), highlighting the aggressiveness of these cell lines.

Osteosarcoma PDX-derived cell lines spontaneously metastasize in an orthotopic amputation model

Postamputation, mice in orthotopic studies were monitored for metastatic burden for up to 6 months using BLI and health monitoring (**Table 3**; **Figs. 5A**, **6A** and **B**; Supplementary Fig. S10A–S10G). Study duration after amputation ranged from one to a maximum of 6 months (**Table 3**; Supplementary Fig. S10A–S10G). Spontaneous metastases developed in mice for five of the seven xenograft forming PDX-derived cell lines with BLI signal increasing over time (**Table 3**; Supplementary Fig. S10A–S10G). BLI signal at endpoint showed a trend of being inversely correlated with time to endpoint (**Table 3**; **Fig. 6A** and **B**) demonstrating that higher metastatic burden causes increased morbidity *in vivo*.

As with the intravenous model described above, there was a high degree of tissue-specific tropism in metastasis development (**Table 3**; **Fig. 6A**). Two of the five metastatic PDX-derived cell lines (OS742 and OS152) metastasized consistently to the lung in all mice (**Table 3**; **Fig. 6C** and **D**). Of the remaining three xenograft-forming cell lines that metastasized, two (OS525 and OS384) metastasized to lung with high frequency (50% and 88%, respectively) and one (OS052) never metastasized to the lung (**Table 3**; **Fig. 6C** and **D**). PDX-derived cell lines OS152, OS525, and OS742 also metastasized to bone (spine, skull, and long bone) as well as liver in up to 100% of mice (**Table 3**; Supplementary Figs. S10H–S10I and S11). Four of the PDX-derived cell lines also metastasized to other soft tissue sites (abdomen, kidney, axillary region, and mediastinum) in 13% to 86% of mice (**Table 3**). Lung burden by area for all mice remained below 4%, whereas liver burden reached as high as nearly 50% (**Fig. 6C**; Supplementary Fig. S11A). The three most aggressive cell lines (OS152, OS742, and OS525) metastasized in all mice with the highest overall burden, to the most sites and with the shortest latency (**Table 3**; **Fig. 6**; Supplementary Figs. S10 and S11) compared with the remaining PDX-derived cell lines. OS052 was one

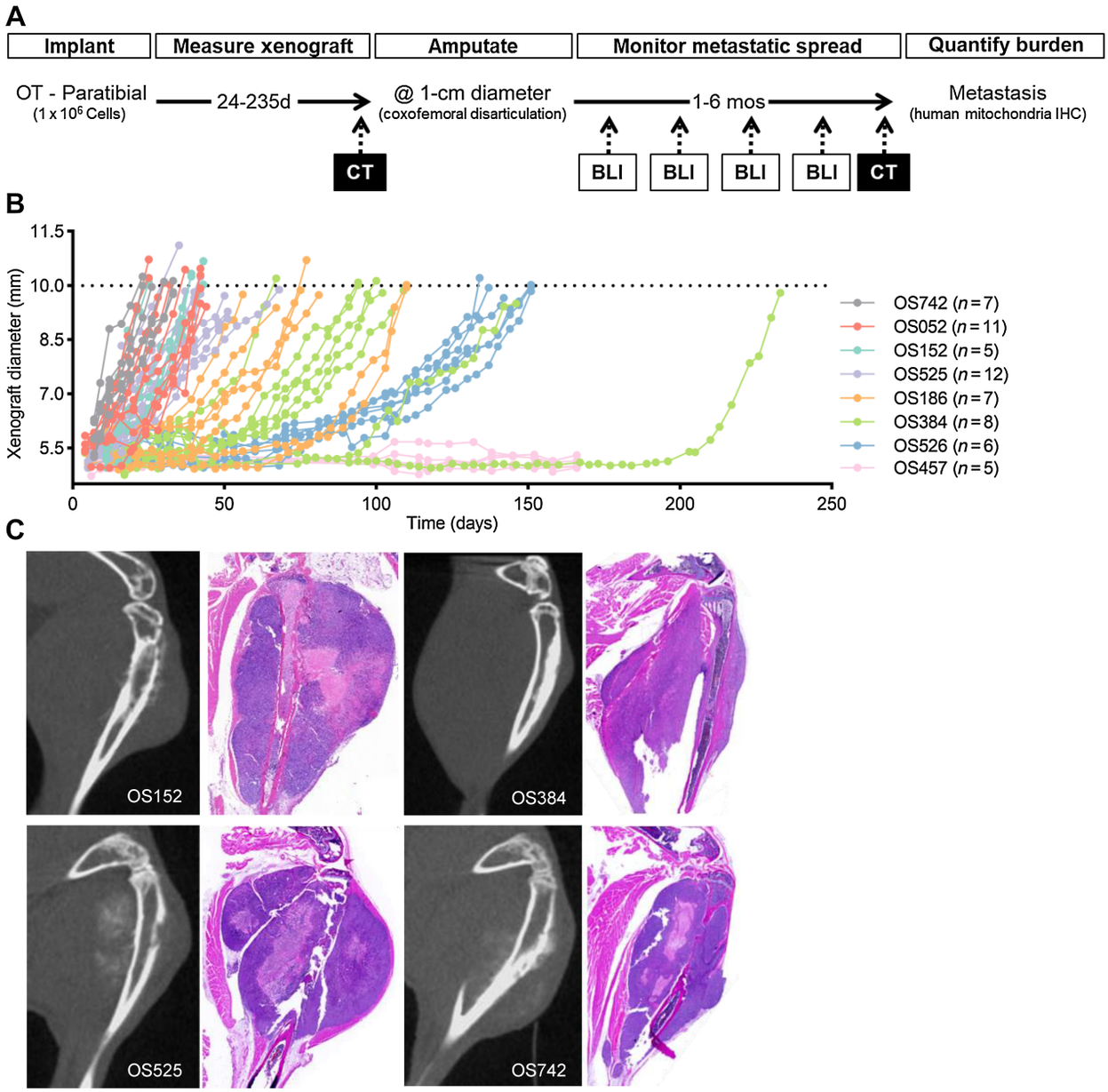

Figure 5.

Osteosarcoma PDX-derived cell lines form invasive xenografts after paratibial orthotopic implantation. **A,** Orthotopic model schematic: 1×10^6 cells were implanted paratibially into the right hindlimb of 2- to 5-month-old NSG mice. Limb diameter was measured bi-weekly until reaching 1 cm when limb microCT was performed, followed by amputation via coxo-femoral disarticulation. After amputation, mouse health was monitored for clinical signs associated with metastasis and BLI was performed monthly to estimate burden and to determine study endpoint for each cell line. At endpoint, tissues were harvested for quantitative burden analysis using human mitochondria IHC. **B,** Bi-weekly xenograft diameter measurements for individual mice implanted with each PDX-derived cell line. Mice implanted with the same cell line tended to require amputation at similar time points. All but one cell line, OS457, formed xenografts that reached 1 cm in diameter. **C,** After paratibial implantation, PDX-derived cell line xenografts invaded through the cortex. Example hindlimb microCTs with corresponding histopathology demonstrating tumor expansion as well as cortical and trabecular bone invasion for several tumorigenic PDX-derived cell lines. Hematoxylin and eosin.

of the fastest cell lines to grow a 1-cm xenograft at the orthotopic site but had low capacity to form spontaneous metastasis (**Table 3**; **Figs. 5B** and **6A** and **B**). Using the orthotopic model, metastatic capacity and site tropism between the luciferase and parental versions were similar (Supplementary Fig. S9E–S9H; Supplementary Table S4).

Performance of established commercial osteosarcoma cell lines using intravenous and orthotopic *in vivo* models

Next, we compared the *in vivo* metastatic phenotypes of the panel of osteosarcoma PDX-derived cell lines to a small subset of commercially available established osteosarcoma cell lines by evaluating them using the same intravenous and orthotopic models described above.

Table 3. Osteosarcoma PDX-derived cell line *in vivo* orthotopic study summary table.

		OS742	OS152	OS525	OS052	OS186	OS384	OS526	OS457
# Mice Total [# Studies]		5 [1]	7 [1]	6 [2]	9 [3]	8 [2]	5 [2]	7 [2]	5 [1]
Amp Time (avg days)		39	30	53	35	119	144	83	N/A
Endpoint (avg days)		29	32	84	168	168	161	168	168
Endpoint Decision with		BLI	BLI, CS	BLI, CS	max	max	max, CS	max	N/A
CS, if Applicable		N/A	abd mass	paralysis	N/A	N/A	low BCS	N/A	N/A
Metastatic Sites (%)	Lung	100	100	50	0	88	N/A	N/A	N/A
	Bone	40	43	100	11	0	—	—	—
	Liver	100	100	50	0	0	—	—	—
	Other	0	86	50	22	13	—	—	—

Abbreviations: abd, abdominal; amp, amputation; avg, average; BCS, body condition score; CS, clinical signs.

In the intravenous model, SJSA and MG63.3 caused metastasis-associated morbidity faster than the most aggressive PDX-derived cell lines; the BLI signal for SJSA at endpoint was comparable to the most aggressive PDX-derived cell lines but in half of the time (Supplementary Table S5; Supplementary Fig. S12A and S12B). The metastatic lung burden for SJSA and MG63.3 was much higher than the PDX-derived cell lines, whereas for MG63 it was lower than many of the PDX-cell derived cell lines (Supplementary Fig. S12C and S12D). Unlike with the PDX-derived cell lines, lung metastases formed by established commercially available osteosarcoma cell lines were more evenly distributed throughout the pulmonary parenchyma (Supplementary Fig. S12E). However, MG63.3 tended to track along large airways and the MG63/MG63.3 tumors appear to contain a reduced number of human mitochondria compared with SJSA or PDX-derived cell line metastases (Supplementary Fig. S12E; **Fig. 4F** and **6E**). None of the established commercially available cell lines metastasized to bone and only SJSA metastasized to the liver (Supplementary Fig. S12F–S12H). Because human osteosarcoma frequently metastasizes to bone, a useful feature of the PDX-derived cell line panel described here is the observed bone tropism.

In the orthotopic model, SJSA and MG63.3 xenografts grew quickly with all mice requiring amputation by one month; for MG63, xenografts were sporadically palpable in some mice, but limb diameter was never much larger than ∼6 mm in diameter, even after >250 days postimplantation (Supplementary Table S6 and Supplementary Fig. S13A and S13B). Like the PDX-derived cell line xenografts, SJSA and MG63.3 xenografts invaded through the tibial cortex (Supplementary Fig. S13C and S13D). For SJSA and MG63.3, study duration from amputation to endpoint (Supplementary Table S6) and metastatic lung burden (Supplementary Fig. S13E–S13I) was similar to the most aggressive PDX-derived cell lines; neither of these cell lines metastasized to bone in the orthotopic model. After comparing the *in vivo* metastatic phenotypes of PDX-derived cell lines to established osteosarcoma cell lines in intravenous and orthotopic models, we next set out to demonstrate their potential utility in genomically informed targeted drug studies.

CDK inhibition with dinaciclib decreases metastasis in *MYC* amplified osteosarcoma *in vivo*

A primary rationale for the development of an osteosarcoma orthotopic amputation model using PDX-derived cell lines that metastasize spontaneously is to use this model to test new therapeutic approaches that may be effective for treatment of metastatic disease. To this end, we tested the response to targeted therapy in one of the PDX-derived cell lines, OS152, which carries a *MYC* amplification (**Table 1**; **Fig. 2**; Supplementary Table S3). MYC expression is higher and there is MYC target gene set enrichment in the *MYC* amplified cell lines (Supplementary Fig. S14). We have previously shown that *MYC* amplified subcutaneous xenografts can be targeted with the CDK inhibitor dinaciclib (11). Dinaciclib inhibits CDK2/5/9 which results in downregulation of MYC expression (75). To determine the utility of this model as a preclinical tool to assess the efficacy of dinaciclib therapy, mice were implanted with OS152 luciferase-expressing cells orthotopically as described above. Intraperitoneal dinaciclib administration (20 mg/kg 5 times/week) commenced 4 days postamputation (**Fig. 7A**). At endpoint, the BLI signal was significantly lower in dinaciclib treated mice ($P = 0.0153$; t test; **Fig. 7C** and **D**) and the difference between the treatment and control groups increased with time (**Fig. 7B**). In the treatment group, there was a significant reduction in the average metastatic tumor area (lung: $P = 0.0315$ and liver: $P = 0.0040$, Mann–Whitney test; **Fig. 7E**) and number of metastases per mm^2 (lung: $P = 0.0024$, t test and liver: $P = 0.0400$, Mann–Whitney test; **Fig. 7F**) in the lung and liver. These results suggest that the orthotopic metastasis model developed here can be used to evaluate novel targeted therapeutic approaches to treat osteosarcoma metastasis.

Discussion

Osteosarcoma remains a major clinical challenge largely due to its propensity to metastasize. While MYC has been suggested to be associated with aggressive disease (76), there are currently no known mechanisms of metastatic spread in osteosarcoma. The paucity of well-characterized metastasis models for this disease limits the ability to identify mechanisms of metastasis as well as the development of therapies specifically directed at preventing or treating metastatic spread. To address this need, we describe the development and characterization of a large panel of PDXs and PDX-derived cell lines which can be used to study osteosarcoma metastasis. We observed that the PDXs and PDX-derived cell lines largely share the genomic features of their original patient tumors and exhibit genomic complexity that mirrors what is observed in the human disease and is distinct from commercially available cell lines. Similarly, transcriptome clustering indicates that the PDXs and PDX-derived cell lines cluster with their tumor of origin, indicating close fidelity that is maintained over time. We also observed that PDX-derived cell lines cluster with the patient of origin samples rather than with other established commercially available cell lines, suggesting a distinct biology and perhaps a closer similarity to the human disease. Overall, the genomic and transcriptomic studies we performed strongly

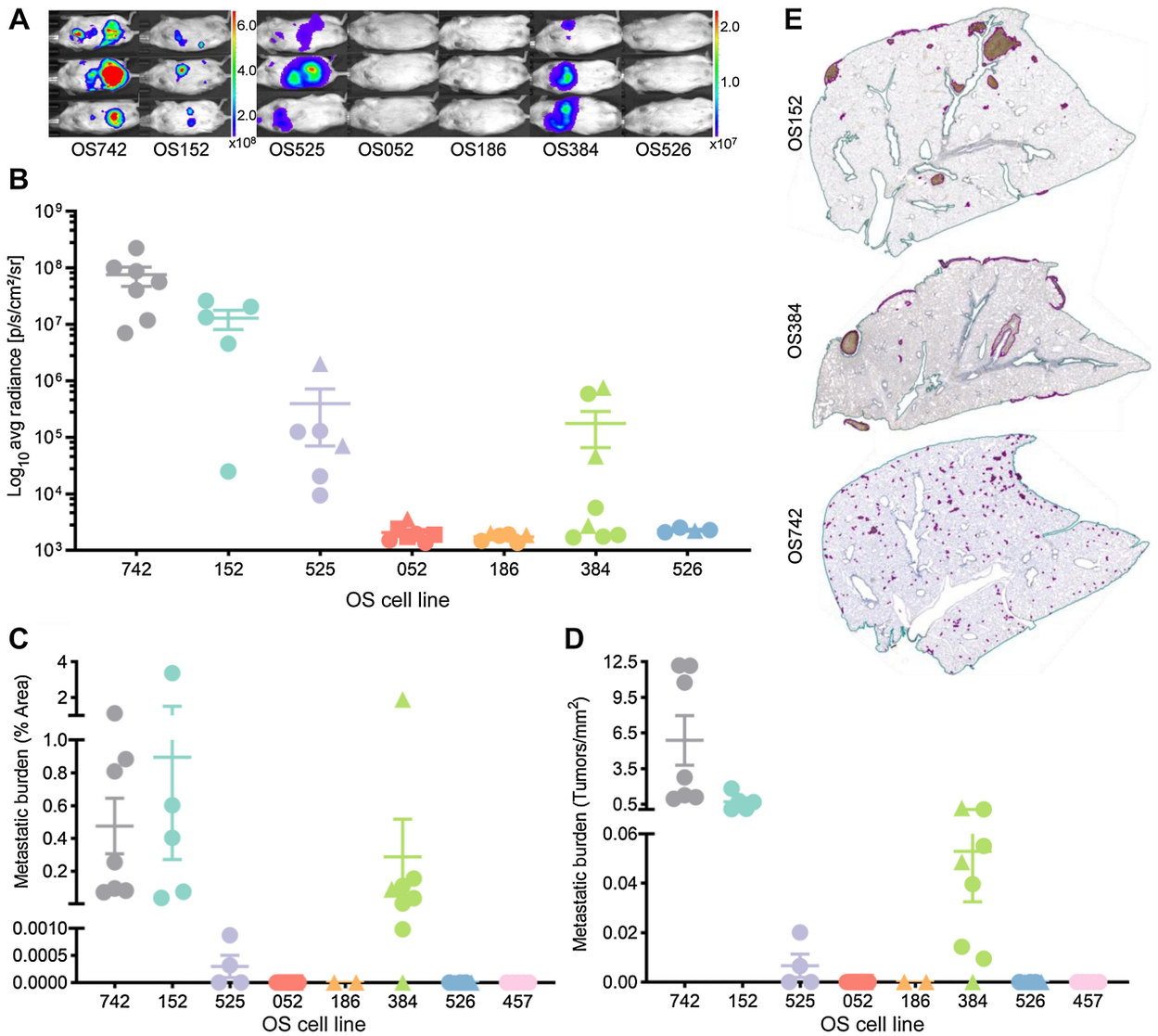

Figure 6.

Osteosarcoma PDX-derived cell lines metastasize spontaneously in an orthotopic amputation model. For all graphs, within each cell line, mice implanted at the same time are represented by the same symbol. **A,** Metastatic burden varied between cell lines. Representative images of the BLI signal at endpoint for each cell line representing total tumor burden from all sites. BLI color scale is in radiance (photons/sec/cm^2/sr); left scale: Min = 1.08×10^8 and Max = 6.62×10^8 and right scale: Min = 2.29×10^5 and Max = 2.29×10^7. **B,** Total BLI signal at endpoint for all mice, ordered from fastest to slowest time to amputation, for each PDX-derived cell line. **C** and **D,** Metastases were observed most consistently in the lung. Metastatic burden quantification of lung tissue immunolabeled with human mitochondria antibody for overall tumor area (**C**) and number of tumors per mm^2 (**D**) for individual mice. **E,** Tumor size and distribution in lung parenchyma varied between cell lines. Microscopic images of lung lobes immunolabeled with human mitochondria antibody demonstrating metastatic burden for three PDX-derived cell lines. Tissue outlined in teal and tumors outlined in purple.

support the significant added value of developing new PDXs and PDX-derived cell lines for rare cancers rather than relying completely on the often-limited number of highly passaged immortal cell lines currently widely available.

We characterized the *in vivo* metastatic characteristics of eight PDX-derived cell lines and demonstrated that they have a wide phenotypic range with regard to primary orthotopic growth and metastatic progression. The PDX-derived cell lines are heterogenous with respect to their tumorigenicity as well as their metastatic propensity and tropism. We anticipate that this will be a particularly useful feature of this resource as it will facilitate the selection of cell lines for the investigation of specific aspects of the osteosarcoma metastatic cascade. Three PDX-derived cell lines (OS742, OS152, and OS525) were found to have a consistently high metastatic capacity whereas two cell lines were non-metastatic (OS457 and OS186), and another three had an intermediate metastatic phenotype (OS052, OS526, and OS384). Of the cell lines tested *in vivo*, OS457 and OS186 were the PDX-derived cell lines most divergent from their patient tumor, due to WGD (Supplementary Fig. S2B). It is possible that this drift has deleterious effects on the *in vivo* growth of these cell lines. PDX-

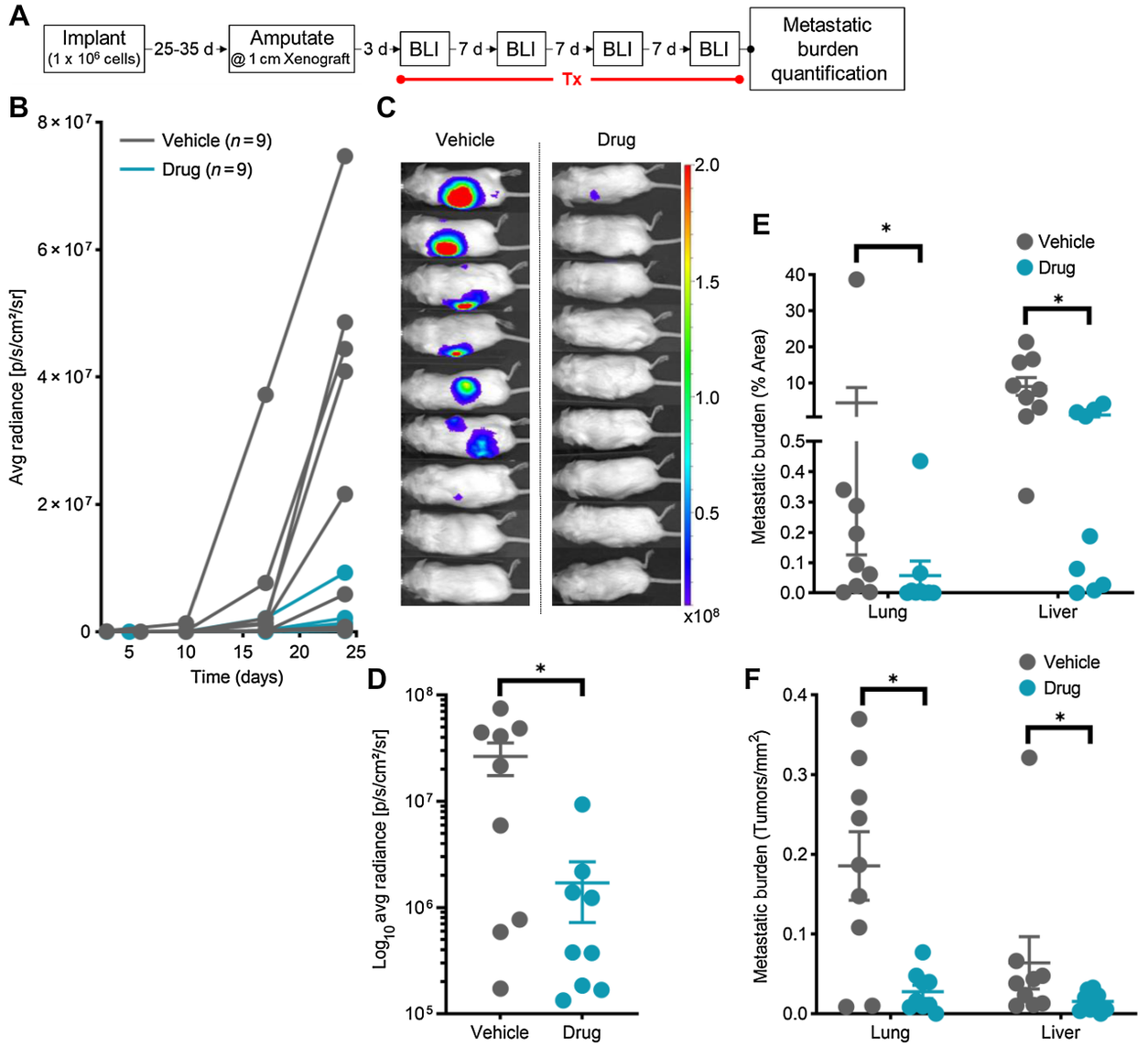

Figure 7.

MYC amplified osteosarcoma metastases generated using an orthotopic amputation mouse model responded to targeted treatment with a CDK2/5/9 inhibitor. **A,** Drug study schematic: orthotopic xenografts were established by implanting 1×10^6 OS152 cells paratibially into 6- to 9-week-old NSG mice. Xenograft diameter was measured biweekly, and the affected limb was amputated at 1 cm in diameter. Dinaciclib treatment (20 mg/kg 5 times/week intraperitoneal) was initiated 4 days postamputation for 3 weeks and BLI was performed weekly to monitor metastatic burden. At endpoint, tissues were harvested for quantitative burden analysis. **B,** Tumor burden increased over time in both groups but was higher in the vehicle only group. Weekly BLI signal for all individual mice over the duration of the study. **C,** At endpoint, metastatic burden was higher in the vehicle only group. BLI signal images for individual mice at endpoint. BLI color scale is in radiance (photons/sec/cm^2/sr). **D,** Total BLI signal at endpoint for all mice representing whole body metastatic burden was significantly lower in treated mice ($P = 0.0153$, t test). **E** and **F,** Tumor burden area (lung: $P = 0.0315$ and liver: $P = 0.0040$, both Mann–Whitney test) and number of tumors per mm^2 (lung: $P = 0.0024$, t test and liver: $P = 0.0400$, Mann–Whitney test) were significantly lower in treated mice. Metastatic burden quantification of lung and liver tissue immunolabeled with human mitochondria antibody for overall tumor area (**E**) and number of tumors per mm^2 (**F**) for individual mice. Error bars represent SEM.

derived cell lines metastasized most frequently to the lungs, which is also the most common metastatic site in patients. Multiple PDX-derived cell lines also metastasize to bone (OS052, OS152, OS525, and OS742), another important metastatic site in patients with osteosarcoma and an essentially non-existent feature in other previously described models, with the exception of the naturally occurring canine model (28, 45). The two most aggressive cell lines (OS152 and OS742) form invasive orthotopic xenografts that reach the amputation endpoint in <6 weeks and metastasize to lung, liver, bone, and other sites less than 1 month postamputation; these latency characteristics make this an appealing model for mechanistic studies and preclinical therapeutic development.

The variation in metastasis predilection sites between osteosarcoma PDX-derived cell lines illustrates the ability of these models to recapitulate the spectrum of the human disease.

In prior work, we demonstrated that the CDK inhibitor dinaciclib leads to decreased subcutaneous xenograft growth for osteosarcoma PDX-derived cell lines that carry *MYC* amplification (11). Here, we assessed whether dinaciclib could be used to decrease the progression of metastasis in an orthotopic amputation model. This proof-of-concept experiment, using one osteosarcoma PDX-derived cell line (OS152), demonstrated that this model can be used effectively to test the effects of targeting genomic features to inhibit metastasis.

The PDX-derived cell lines described here were derived from both primary and metastatic sites. We did not find a clear association between patient of origin metastatic disease status and the *in vivo* metastatic phenotype or xenograft growth of the PDX-derived cell lines. The PDX-derived cell line exhibiting the fastest xenograft growth (OS742) and the non-tumorigenic cell line (OS457) were both derived from primary tumors. Similarly, of the two most metastatic cell lines, one is primary in origin (OS742) and the other originates from a metastatic site (OS152). The established commercially available osteosarcoma cell lines evaluated here were all derived from primary tumors and were either highly tumorigenic and produced heavy metastatic burden (MG63.3 and SJSA) or were non-tumorigenic and produced minimal metastatic burden (MG63). For SJSA and MG63.3, especially in the intravenous model, the metastatic burden induced in a short timeframe (∼1 month), caused significant morbidity in the mice and presented challenges with burden quantification.

In patients, conventional osteosarcoma most commonly originates centrally in the metaphyseal region. In our orthotopic model, cells are implanted paratibially to avoid direct seeding into the bloodstream via the bone marrow. However, pre-amputation microCT and postamputation histologic examination of the affected limbs confirmed that all cell lines capable of forming xenografts also invade through the cortex. Confirming central invasion of the osteosarcoma PDX-derived cell line xenografts is probably critical for more accurate modeling of the human disease. In PDX paratibial implantation amputation models, metastasis incidence is reported to be lower in the mouse model than in human patients, ranging from 25% to 50% between PDXs (41, 51). Using PDX-derived cell lines in the orthotopic model, we achieved metastatic rates that were more in line with patient outcome; in three PDX cell lines, the metastatic rate was 100% and a fourth cell line reached 88% in the orthotopic model. In summary, we describe here a panel of new osteosarcoma PDX-derived cell lines that we believe will be of wide use to the osteosarcoma research community.

Authors' Disclosures

C.R. Schott reports a grant from Rally Foundation for Childhood Cancer Research during the conduct of the study. C. Curtis reports personal fees from NanoString, Genentech, ResistanceBio, Bristol-Myers Squibb, 3T Biosciences; and personal fees from DeepCell outside the submitted work. E.A. Sweet-Cordero reports grants from NCI and St Baldricks Foundation; as well as grants from Hyundai Hope on Wheels during the conduct of the study. No disclosures were reported by the other authors.

Disclaimer

The content is solely the responsibility of the authors and does not necessarily represent the official views of the NIH.

Authors' Contributions

C.R. Schott: Conceptualization, formal analysis, supervision, validation, investigation, visualization, methodology, writing–original draft, project administration, writing–review and editing. **A.L. Koehne:** Conceptualization, investigation, methodology. **L.C. Sayles:** Conceptualization, data curation, methodology, writing–review and editing. **E.P. Young:** Investigation. **C. Luck:** Formal analysis, visualization, methodology. **K. Yu:** Resources. **A.G. Lee:** Resources, data curation, formal analysis, visualization, methodology. **M.R. Breese:** Resources, data curation, formal analysis, visualization, methodology. **S.G. Leung:** Sample acquisition, acquired patient consent. **H. Xu:** Formal analysis, visualization. **A.T. Shah:** Data curation. **H.-Y. Liu:** Sample acquisition, acquired patient consent. **A. Spillinger:** Sample acquisition, acquired patient consent. **I.H. Behroozfard:** Sample acquisition, acquired patient consent. **K.D. Marini:** Investigation. **P.T. Dinh:** Sample acquisition, acquired patient consent. **M.V. Pons Ventura:** Sample acquisition, acquired patient consent. **E.N. Vanderboon:** Formal analysis. **F.K. Hazard:** Confirmed the diagnosis of osteosarcoma in patient samples. **S.-J. Cho:** Confirmed the diagnosis of osteosarcoma in patient samples. **R.S. Avedian:** Sample acquisition. **D.G. Mohler:** Sample acquisition. **M. Zimel:** Sample acquisition. **R. Wustrack:** Sample acquisition. **C. Curtis:** Resources. **M. Sirota:** Resources. **E.A. Sweet-Cordero:** Conceptualization, resources, supervision, funding acquisition, validation, writing–original draft, project administration.

Acknowledgments

We thank the members of the UCSF Helen Diller Family Comprehensive Cancer Center (HDFCCC) Preclinical Therapeutics Core and Animal Care at UCSF for their useful advice throughout the development of this project. Sequencing was performed at the UCSF Center for Advanced Technology (CAT), supported by UCSF PBBR, RRP IMIA, and NIH 1S10OD028511–01 grants. This work was also supported by NIH S10 instrument grant S10OD025022. Cell sorting was performed at the UCSF Laboratory for Cell Analysis (LCA), supported by the NCI of the NIH under Award Number P30CA082103. C.R. Schott was supported by a Postdoctoral Research Fellow Grant from the Rally Foundation for Childhood Cancer Research. E.A. Sweet-Cordero was supported by the NIH (1R01CA243555) and by the Battle Osteosarcoma grant from the St. Baldrick's Foundation. Dr. Hani Goodarzi gifted the luciferase plasmid. Dr. Robbie Majzner of Stanford University gifted cell line MG63.3. Sara Pyle generated the graphical abstract (**Fig. 1**). We thank especially all the patients and their families who generously consented to tissue donation to enable this work.

The publication costs of this article were defrayed in part by the payment of publication fees. Therefore, and solely to indicate this fact, this article is hereby marked "advertisement" in accordance with 18 USC section 1734.

Note

Supplementary data for this article are available at Clinical Cancer Research Online (http://clincancerres.aacrjournals.org/).

Received March 21, 2023; revised March 26, 2023; accepted August 8, 2023; published first September 13, 2023.

References

1. Meyers PA. Malignant bone tumors in children: osteosarcoma. Hematol Oncol Clin North Am 1987;1:655–65.
2. Collier CD, Wirtz EC, Knafler GJ, Morris WZ, Getty PJ, Greenfield EM. Micrometastatic drug screening platform shows heterogeneous response to MAP chemotherapy in osteosarcoma cell lines. Clin Orthop Relat Res 2018; 476:1400–11.
3. Luetke A, Meyers PA, Lewis I, Juergens H. Osteosarcoma treatment - where do we stand? A state of the art review. Cancer Treat Rev 2014;40: 523–32.
4. Bielack SS, Kempf-Bielack B, Delling G, Exner GU, Flege S, Helmke K, et al. Prognostic factors in high-grade osteosarcoma of the extremities or trunk: an analysis of 1,702 patients treated on neoadjuvant cooperative osteosarcoma study group protocols. J Clin Oncol 2002;20: 776–90.
5. Kager L, Zoubek A, Pötschger U, Kastner U, Flege S, Kempf-Bielack B, et al. Primary metastatic osteosarcoma: presentation and outcome of patients treated on neoadjuvant cooperative osteosarcoma study group protocols. J Clin Oncol 2003;21:2011–8.

6. Marina NM, Smeland S, Bielack SS, Bernstein M, Jovic G, Krailo MD, et al. Comparison of MAPIE versus MAP in patients with a poor response to preoperative chemotherapy for newly diagnosed high-grade osteosarcoma (EURAMOS-1): an open-label, international, randomized controlled trial. Lancet Oncol 2016;17:1396–408.
7. Meltzer PS, Helman LJ. New horizons in the treatment of osteosarcoma. N Engl J Med 2021;385:2066–76.
8. Lilienthal I, Herold N. Targeting molecular mechanisms underlying treatment efficacy and resistance in osteosarcoma: a review of current and future strategies. Int J Mol Sci 2020;21:1–56.
9. Roberts RD, Lizardo MM, Reed DR, Hingorani P, Glover J, Allen-Rhoades W, et al. Provocative questions in osteosarcoma basic and translational biology: a report from the Children's Oncology Group. Cancer. 2019;125:3514–25.
10. Khanna C, Fan TM, Gorlick R, Helman LJ, Kleinerman ES, Adamson PC, et al. Toward a drug development path that targets metastatic progression in osteosarcoma. Clin Cancer Res 2014;20:4200–9.
11. Sayles LC, Breese MR, Koehne AL, Leung SG, Lee AG, Liu H-Y, et al. Genome-informed targeted therapy for osteosarcoma. Cancer Discov 2019;9:46–63.
12. Ren L, Mendoza A, Zhu J, Briggs JW, Halsey C, Hong ES, et al. Characterization of the metastatic phenotype of a panel of established osteosarcoma cells. Oncotarget 2015;6:29469–81.
13. Manara MC, Baldini N, Serra M, Lollini PL, De Giovanni C, Vaccari M, et al. Reversal of malignant phenotype in human osteosarcoma cells transduced with the alkaline phosphatase gene. Bone 2000;26:215–20.
14. Jia SF, Worth LL, Kleinerman ES. A nude mouse model of human osteosarcoma lung metastases for evaluating new therapeutic strategies. Clin Exp Metastasis 1999;17:501–6.
15. Duan X, Jia S-F, Zhou Z, Langley RR, Bolontrade MF, Kleinerman ES. Association of alphavbeta3 integrin expression with the metastatic potential and migratory and chemotactic ability of human osteosarcoma cells. Clin Exp Metastasis 2004;21:747–53.
16. Zhang Y, Zvi YS, Batko B, Zaphiros N, O'Donnell EF, Wang J, et al. Down-regulation of Skp2 expression inhibits invasion and lung metastasis in osteosarcoma. Sci Rep 2018;8:14294.
17. Morrow JJ, Bayles I, Funnell APW, Miller TE, Saiakhova A, Lizardo MM, et al. Positively selected enhancer elements endow osteosarcoma cells with metastatic competence. Nat Med 2018;24:176–85.
18. Bayles I, Krajewska M, Pontius WD, Saiakhova A, Morrow JJ, Bartels C, et al. *Ex vivo* screen identifies CDK12 as a metastatic vulnerability in osteosarcoma. J Clin Invest 2019;129:4377–92.
19. Xu WT, Bian ZY, Fan QM, Li G, Tang TT. Human mesenchymal stem cells (hMSCs) target osteosarcoma and promote its growth and pulmonary metastasis. Cancer Lett 2009;281:32–41.
20. Tiram G, Segal E, Krivitsky A, Shreberk-Hassidim R, Ferber S, Ofek P, et al. Identification of dormancy-associated microRNAs for the design of osteosarcoma-targeted dendritic polyglycerol nanopolyplexes. ACS Nano 2016;10:2028–45.
21. Rhim JS, Park DK, Arnstein P, Huebner RJ, Weisburger EK, Nelson-Rees WA. Transformation of human cells in culture by N-methyl-N'-nitro-N-nitrosoguanidine. Nature 1975;256:751–3.
22. Rhim JS, Putman DL, Arnstein P, Huebner RJ, McAllister RM. Characterization of human cells transformed *in vitro* by N-methyl-N'-nitro-N-nitrosoguanidine. Int J cancer 1977;19:505–10.
23. Samid D, Mandler R. Human osteosarcoma cells transformed by ras-oncogenes: a new model for *in vivo* studies of pulmonary metastasis. Clin Biotechnol 1989;1:21–6.
24. Asai T, Ueda T, Itoh K, Yoshioka K, Aoki Y, Mori S, et al. Establishment and characterization of a murine osteosarcoma cell line (LM8) with high metastatic potential to the lung. Int J cancer 1998;76:418–22.
25. Kimura K, Nakano T, Park Y-B, Tani M, Tsuda H, Beppu Y, et al. Establishment of human osteosarcoma cell lines with high metastatic potential to lungs and their utilities for therapeutic studies on metastatic osteosarcoma. Clin Exp Metastasis 2002;19:477–85.
26. Nakano T, Tani M, Ishibashi Y, Kimura K, Park Y-B, Imaizumi N, et al. Biological properties and gene expression associated with metastatic potential of human osteosarcoma. Clin Exp Metastasis 2003;20:665–74.
27. Su Y, Luo X, He B-C, Wang Y, Chen L, Zuo G-W, et al. Establishment and characterization of a new highly metastatic human osteosarcoma cell line. Clin Exp Metastasis 2009;26:599–610.
28. Uluçkan Ö, Segaliny A, Botter S, Santiago JM, Mutsaers AJ. Preclinical mouse models of osteosarcoma. Bonekey Rep 2015;4:670.
29. Yuan J, Ossendorf C, Szatkowski JP, Bronk JT, Maran A, Yaszemski M, et al. Osteoblastic and osteolytic human osteosarcomas can be studied with a new xenograft mouse model producing spontaneous metastases. Cancer Invest 2009;27:435–42.
30. Luu HH, Kang Q, Jong KP, Si W, Luo Q, Jiang W, et al. An orthotopic model of human osteosarcoma growth and spontaneous pulmonary metastasis. Clin Exp Metastasis 2005;22:319–29.
31. Nomura M, Rainusso N, Lee Y, Dawson B, Coarfa C, Han R, et al. Tegavivint and the β-catenin/ALDH axis in chemotherapy-resistant and metastatic osteosarcoma. J Natl Cancer Inst 2019;111:1–12.
32. Majzner RG, Theruvath JL, Nellan A, Heitzeneder S, Cui Y, Mount CW, et al. CAR T cells targeting B7-H3, a pan-cancer antigen, demonstrate potent preclinical activity against pediatric solid tumors and brain tumors. Clin cancer Res 2019;25:2560–74.
33. Husmann K, Arlt MJE, Muff R, Langsam B, Bertz J, Born W, et al. Matrix metalloproteinase 1 promotes tumor formation and lung metastasis in an intratibial injection osteosarcoma mouse model. Biochim Biophys Acta 2013;1832:347–54.
34. Butch ER, Mead PE, Amador Diaz V, Tillman H, Stewart E, Mishra JK, et al. Positron emission tomography detects *in vivo* expression of disialoganglioside GD2 in mouse models of primary and metastatic osteosarcoma. Cancer Res 2019;79:3112–24.
35. Zhang T, Li S, Li J, Yin F, Hua Y, Wang Z, et al. Natural product pectolinarigenin inhibits osteosarcoma growth and metastasis via SHP-1–mediated STAT3 signaling inhibition. Cell Death Dis 2016;7:e2421.
36. Sabile AA, Arlt MJE, Muff R, Bode B, Langsam B, Bertz J, et al. Cyr61 expression in osteosarcoma indicates poor prognosis and promotes intratibial growth and lung metastasis in mice. J Bone Miner Res 2012;27:58–67.
37. Broadhead ML, Dass CR, Choong PFM. Systemically administered PEDF against primary and secondary tumors in a clinically relevant osteosarcoma model. Br J Cancer 2011;105:1503–11.
38. Igarashi K, Kawaguchi K, Kiyuna T, Miyake K, Murakami T, Yamamoto N, et al. Effective metabolic targeting of human osteosarcoma cells *in vitro* and in orthotopic nude-mouse models with recombinant methioninase. Anticancer Res 2017;37:4807–12.
39. Berlin O, Samid D, Donthineni-Rao R, Akeson W, Amiel D, Woods VL. Development of a novel spontaneous metastasis model of human osteosarcoma transplanted orthotopically into bone of athymic mice. Cancer Res 1993;53:4890–5.
40. Eikenes L, Tari M, Tufto I, Bruland OS, de Lange Davies C. Hyaluronidase induces a transcapillary pressure gradient and improves the distribution and uptake of liposomal doxorubicin (Caelyx) in human osteosarcoma xenografts. Br J Cancer 2005;93:81–8.
41. Goldstein SD, Hayashi M, Albert CM, Jackson KW, Loeb DM. An orthotopic xenograft model with survival hindlimb amputation allows investigation of the effect of tumor microenvironment on sarcoma metastasis. Clin Exp Metastasis 2015;32:703–15.
42. Loh AHP, Stewart E, Bradley CL, Chen X, Daryani V, Stewart CF, et al. Combinatorial screening using orthotopic patient derived xenograft-expanded early phase cultures of osteosarcoma identify novel therapeutic drug combinations. Cancer Lett 2019;442:262–70.
43. Maloney C, Edelman MC, Kallis MP, Soffer SZ, Symons M, Steinberg BM. Intratibial injection causes direct pulmonary seeding of osteosarcoma cells and is not a spontaneous model of metastasis: a mouse osteosarcoma model. Clin Orthop Relat Res 2018;476:1514–22.
44. Hildreth BE, Palmer C, Allen MJ. Modeling primary bone tumors and bone metastasis with solid tumor graft implantation into bone. J Vis Exp 2020;1–13.
45. Beck J, Ren L, Huang S, Berger E, Bardales K, Mannheimer J, et al. Canine and murine models of osteosarcoma. Vet Pathol 2022;59:399–414.
46. Stewart E, Federico SM, Chen X, Shelat AA, Bradley C, Gordon B, et al. Orthotopic patient-derived xenografts of pediatric solid tumors. Nature 2017;549:96–100.
47. Meohas W, Granato RA, Guimarães JAM, Dias RB, Fortuna-Costa A, Duarte MEL. Patient-derived xenografts as a preclinical model for bone sarcomas. Acta Ortop Bras 2018;26:98–102.
48. Rainusso N, Cleveland H, Hernandez JA, Quintanilla NM, Hicks J, Vasudevan S, et al. Generation of patient-derived tumor xenografts from percutaneous tumor biopsies in children with bone sarcomas. Pediatr Blood Cancer 2019;66:e27579.
49. Rokita JL, Rathi KS, Cardenas MF, Upton KA, Jayaseelan J, Cross KL, et al. Genomic profiling of childhood tumor patient-derived xenograft models to enable rational clinical trial design. Cell Rep 2019;29:1675–89.

50. Crnalic S, Hakansson I, Boquist L, Lofvenberg R, Brostrom LA. A novel spontaneous metastasis model of human osteosarcoma developed us7ng orthotopic transplantation of intact tumor tissue into tibia of nude mice. Clin Exp Metastasis 1997;15:164–72.
51. Goldstein SD, Trucco M, Bautista Guzman W, Hayashi M, Loeb DM. A monoclonal antibody against the Wnt signaling inhibitor dickkopf-1 inhibits osteosarcoma metastasis in a preclinical model. Oncotarget 2016;7:21114–23.
52. Landuzzi L, Manara MC, Lollini P-L, Scotlandi K. Patient derived xenografts for genome-driven therapy of osteosarcoma. Cells 2021;10:1–18.
53. Dobin A, Davis CA, Schlesinger F, Drenkow J, Zaleski C, Jha S, et al. STAR: ultrafast universal RNA-seq aligner. Bioinformatics 2013;29:15–21.
54. Robinson MD, McCarthy DJ, Smyth GK. edgeR: a bioconductor package for differential expression analysis of digital gene expression data. Bioinformatics 2010;26:139–40.
55. Leek JT, Johnson WE, Parker HS, Jaffe AE, Storey JD. The sva package for removing batch effects and other unwanted variation in high-throughput experiments. Bioinformatics 2012;28:882–3.
56. Vivian J, Rao AA, Nothaft FA, Ketchum C, Armstrong J, Novak A, et al. Toil enables reproducible, open source, big biomedical data analyses. Nat Biotechnol 2017;35:314–6.
57. Law CW, Chen Y, Shi W, Smyth GK. voom: precision weights unlock linear model analysis tools for RNA-seq read counts. Genome Biol 2014; 15:R29.
58. Korotkevich G, Sukhov V, Budin N, Shpak B, Artyomov MN, Sergushichev A. Fast gene set enrichment analysis. Biorxiv 2021.
59. Yu K, Chen B, Aran D, Charalel J, Yau C, Wolf DM, et al. Comprehensive transcriptomic analysis of cell lines as models of primary tumors across 22 tumor types. Nat Commun 2019;10:3574.
60. Cheng DT, Mitchell TN, Zehir A, Shah RH, Benayed R, Syed A, et al. Memorial Sloan Kettering—integrated mutation profiling of actionable cancer targets (MSK-IMPACT): a hybridization capture-based next-generation sequencing clinical assay for solid tumor molecular oncology. J Mol Diagnostics 2015;17: 251–64.
61. Mody RJ, Wu YM, Lonigro RJ, Cao X, Roychowdhury S, Vats P, et al. Integrative clinical sequencing in the management of refractory or relapsed cancer in youth. JAMA - J Am Med Assoc 2015;314:913–25.
62. Wagner AH, Coffman AC, Ainscough BJ, Spies NC, Skidmore ZL, Campbell KM, et al. DGIdb 2.0: mining clinically relevant drug–gene interactions. Nucleic Acids Res 2016;44:D1036–1044.
63. Cibulskis K, Lawrence MS, Carter SL, Sivachenko A, Jaffe D, Sougnez C, et al. Sensitive detection of somatic point mutations in impure and heterogeneous cancer samples. Nat Biotechnol 2013;31:213–9.
64. Benjamin D, Sato T, Cibulskis K, Getz G, Stewart C, Lichtenstein L. Calling somatic SNVs and indels with Mutect2. Biorxiv 2019;861054.
65. Saunders CT, Wong WSW, Swamy S, Becq J, Murray LJ, Cheetham RK. Strelka: accurate somatic small-variant calling from sequenced tumor-normal sample pairs. Bioinformatics 2012;28:1811–7.
66. Chen X, Schulz-Trieglaff O, Shaw R, Barnes B, Schlesinger F, Källberg M, et al. Manta: rapid detection of structural variants and indels for germline and cancer sequencing applications. Bioinformatics 2016;32:1220–2.
67. Rausch T, Zichner T, Schlattl A, Stütz AM, Benes V, Korbel JO. DELLY: structural variant discovery by integrated paired-end and split-read analysis. Bioinformatics 2012;28:333–9.
68. Cameron DL, Baber J, Shale C, Valle-Inclan JE, Besselink N, van Hoeck A, et al. GRIDSS2: comprehensive characterization of somatic structural variation using single breakend variants and structural variant phasing. Genome Biol 2021;22:1–25.
69. Wala JA, Bandopadhayay P, Greenwald NF, O'Rourke R, Sharpe T, Stewart C, et al. SvABA: genome-wide detection of structural variants and indels by local assembly. Genome Res 2018;28:581–91.
70. Van Loo P, Nordgard SH, Lingjærde OC, Russnes HG, Rye IH, Sun W, et al. Allele-specific copy-number analysis of tumors. Proc Natl Acad Sci USA 2010; 107:16910–5.
71. Raine KM, Van Loo P, Wedge DC, Jones D, Menzies A, Butler AP, et al. ascatNgs: identifying somatically acquired copy-number alterations from whole-genome sequencing data. Curr Protoc Bioinforma 2016;56:15.9.1–15.9.17.
72. Team RC. R: A language and environment for statistical computing. 2020.
73. Department of Health, Education, and Welfare. The Belmont Report. Ethical principles and guidelines for the protection of human subjects of research. J Am Coll Dent 2014;81:4–13.
74. Negri GL, Grande BM, Delaidelli A, El-Naggar A, Cochrane D, Lau CC, et al. Integrative genomic analysis of matched primary and metastatic pediatric osteosarcoma. J Pathol 2019;249:319–31.
75. Carey JPW, Karakas C, Bui T, Chen X, Vijayaraghavan S, Zhao Y, et al. Synthetic lethality of PARP inhibitors in combination with MYC blockade is independent of BRCA status in triple-negative breast cancer. Cancer Res 2018;78:742–57.
76. Feng W, Dean DC, Hornicek FJ, Spentzos D, Hoffman RM, Shi H, et al. Myc is a prognostic biomarker and potential therapeutic target in osteosarcoma. Ther Adv Med Oncol 2020;12:1758835920922055.